Evaluation of Green's Functions for PEEC Models in the Air and Lossy-Ground Space

Ruihan Qi[1] Yuxuan Ding[2], Y. Du[2*], and Mingli Chen[2], Zhe Li[3]

[1]State Key Laboratory of HVDC technology, China Southern Power Grid Research Institute, Guangzhou, China

[2]Dept. of Building Services Engineering, the Hong Kong Polytechnic University, Hung Hom, Kowloon, Hong Kong

[3]Shenzhen Power Supply Bureau, China Southern Power Grid Company Ltd., Shenzhen, China

*ya-ping.du@polyu.edu.hk

Abstract — **This paper presents the numerical evaluation of Green's functions for the generalized PEEC formulation in the air and lossy-ground space. Both the source and field points can be located in any layer of the air-ground space. Green's functions are expressed using Sommerfeld integrals (SIs), which have highly oscillating and slowly decaying integrands. As a robust and easy-implemented approach, the direct real-axis integration is presented with the techniques for removing the singularity and accelerating the convergence. Closed-form expressions are derived for the quasi-static and asymptotic approximation of SIs. The results are compared with NEC2, and good agreements were observed. An image model is developed for quasi-static SIs. The Greens' functions can then be contributed by the source and/or its image. This model is used to derive the frequency-invariant PEEC model for fast transient simulation in the time domain. The proposed numerical procedure can be applied to generate lookup tables of SIs, which are indispensable in the evaluation of PEEC circuit parameters for massive wire segments.**

Keywords — **PEEC, Green's function, lossy ground, quasi-static model, lightning**

1. INTRODUCTION

The partial element equivalent circuit method (PEEC) is one of the electromagnetic modeling approaches for 3D structures [1-2]. It is originally proposed by Ruehli [3] for the inductance calculation of the ultra-large-scale integrated circuit. Now it has been applied in a variety of fields, including the lightning transients in a wire or plate structure [4-11]. In this method, wire segments are represented with circuit components, such as partial inductances and coefficients of potential. Note that these parameters are evaluated with Green's functions. For the wires under the ground or in the air close to the ground, the free-space Green's function is not applicable in the lightning transient analysis. A quick and simple approach for evaluating Green's functions in the air and lossy-ground space is indispensable.

Green's functions for stratified media are normally expressed with Sommerfeld Integrals (SIs). Because of dense oscillations and slow decay of the integrands, evaluation of these SIs becomes a difficult job, and has been significantly addressed in the past decades. In [12] a tutorial introduction is presented for the SIs and their evaluation. The most simple and accurate approach is the direct calculation of these integrals. In [13-15], real-axis integration approaches were introduced to evaluate Green's functions in the air. A special transformation technique was employed to deal with strong oscillation around the branch point on the real axis, and an asymptotic and singularity subtraction technique was employed for convergence acceleration. Other methods have also been proposed to avoid the integration over poles and branch points of the integrand, such as the integration path deformation in the complex plane [16-17]. This technique has been adopted to generate 2D lookup tables of Sommerfeld integrals for both E and H fields in NEC2 [18]. In this method, different integration paths were selected to deal with field points at different locations [18-19]. Several extrapolation methods have been proposed to accelerating Sommerfeld integral tails, including the Shank transformation and weighted average algorithm [20-21]. Another similar approach is the steepest descent path (SDP) method [22-25]. It is particularly used to compute Green's functions in the far-field zone for both source and field points in the air [25]. In this approach, the steepest descent path (SDP) for a saddle point is identified, and the integration is taken along this SDP instead of the Sommerfeld integration path.

The discrete complex image method (DCIM) is an alternative approach for the numerical evaluation of Green's functions. In this method, the integrand is approximated with a set of complex exponential terms in the spectral domain. Spatial-domain Green's functions then are obtained analytically with this set of exponential terms [26-27]. A special technique has been considered in [28] to generate a 3D table for source and field points located in different layers. To improve the accuracy in the near-field and far-field regions, two-level and later three-level DCIM schemes were proposed to capture certain singularities [29-34], particularly for source and field points in the same layers. In this approach, both quasi-static and far-field terms are extracted, and the residual is approximated by the generalized pencil of functions matrix method. Alternative techniques have also be developed, such as the rational function fitting approach [35]. This method has been successfully applied to evaluate Green's functions in stratified media.

When the PEEC method is adopted to analyze lightning transients in wire/plate structures in the air and lossy-ground space, it is necessary to evaluate Green's functions for both vector and scalar potentials for source and field points in any of these two layers. A robust and easy-implemented approach then is required to generate lookup tables. This will facilitate the efficient calculation of the inductance and capacitance of a large set of wire segments for fast transient analysis [4-11]. Such an issue, however, has not been systematically addressed. This paper presents a robust evaluation of these Green's functions in the planar two-layer space of air and lossy ground.

A complete set of formulas are provided for easy implementation of this approach. A frequency-invariant image model also is derived for wire modeling at low frequency, subsequently for efficient PEEC simulation of transients, including lightning transients [36-37]. In Section II, generalized expressions of these Green's functions are presented using the SIs. Section III describes the direct real-axis integration approach together with the techniques for removing the singularity and accelerating the convergence. Section IV presents the quasi-static and asymptotic expressions of SIs. Numerical evaluation of SIs finally are presented in Section V. The comparison with the module adopted in NEC2 is made, as well as the closed-form expressions for both quasi-static and far-field zones. Finally, an application for the PEEC-based transient analysis in a simple circuit is presented.

II. Green's Functions in the Generalized PEEC Model

Shown in Fig. 1 is the configuration of wires situated in the air above lossy ground. The 2-layer medium is characterized by the permittivity ϵ_i and permeability μ_i and conductivity σ_i $(i = 1, 2)$. Note $\epsilon_2 = \epsilon_0$, $\mu_2 = \mu_0$ and $\sigma_2 = 0$ in the air and $\mu_1 = \mu_0$ in the ground. A PEEC model for the wires in the air only was presented in [37] using branch current I and node scalar potential ϕ. With the mixed potential equations in [38-40], the model can be extended to the case in which the source and segments are situated in different layers.

The mixed potential integral equations for field and source points in layers s and f $(s, f = 1 \text{ or } 2)$ [38] are given by

$$\begin{aligned} &R_w \boldsymbol{I}(r) + j\omega \int \overline{\overline{\boldsymbol{G}}}_A^{fs}(r,r') \cdot \boldsymbol{I}(r')dl' = \nabla\phi(r) \\ &\phi(r) = \int K_\phi^{fs}(r,r')\tau(r')dl' + j\omega \int P^{fs}(r,r')\hat{z} \cdot \boldsymbol{I}(r')dl' \end{aligned} \tag{1}$$

where $\overline{\overline{\boldsymbol{G}}}_A^{fs}$ and K_ϕ^{fs} denote respectively the dyadic and scalar Green's functions. P^{fs} is a correction factor for satisfying Lorentz's gauge in the 2-layer medium. R_w is the wire resistance. τ is the line charge density. The corresponding PEEC equations for current segment n and potential segment (node) m are expressed by [37,39-40]

$$\begin{aligned} &\phi_{m+1} - \phi_m = R_{w,n} I_n + \sum_i j\omega L_{ni} I_i \\ &I_{c,m} = \frac{1}{p_{mm}} j\omega\phi_m - \sum_{i \neq m} \frac{p_{mi}}{p_{mm}} I_{c,i} - \sum_i \frac{(j\omega)^2 c_{mi}}{p_{mm}} I_i \end{aligned} \tag{2}$$

where I_n and $I_{c,m}$ are respectively the inductive (branch) and capacitive (node) currents. Note that $I_{c,m} = d(\tau \Delta l_m)/dt$, where Δl_m is the length of a segment l_m. The corresponding circuit model is illustrated in Fig. 2. The circuit parameters L_{ni}, p_{mi} and c_{mi} in (2) are given by

$$\begin{aligned} L_{ni} &= \int_{l_n} \int_{l_i} \overline{\overline{\mathbf{G}}}_A^{fs}(r,r') \cdot d\boldsymbol{l}_i' \cdot d\boldsymbol{l}_n \\ p_{mi} &= \frac{1}{\Delta l_i \Delta l_m} \int_{l_m} \int_{l_i} K_\phi^{fs}(r,r')dl_i dl_m \\ c_{mi} &= \frac{1}{\Delta l_m} \int_{l_m} \int_{l_i} P^{fs}(r,r')\hat{z} \cdot d\boldsymbol{l}_i' dl_m \end{aligned} \tag{3}$$

The dyadic green's function can be decoupled into a set of scalar functions, as follows:

$$\overline{\overline{\boldsymbol{G}}}_A^{fs} = G_{tt}^{fs}\hat{t}\hat{t} + G_{zz}^{fs}\hat{z}\hat{z} + G_{zt}^{fs}\hat{z}\hat{t} \tag{4}$$

where $\hat{t}$ is the unit vector of a current dipole projected on the xy plane. These components together with K_ϕ^{fs} and P^{fs} were derived in [40-41], and can be expressed using Sommerfeld Integrals (SI), as follows:

$$\begin{aligned} G_{tt}^{fs}(r,r') &= \mu_0/4\pi [T^{fs}(r,r') + U^{fs}(r,r')] \\ G_{zz}^{fs}(r,r') &= \mu_0/4\pi [T^{fs}(r,r') + V^{fs}(r,r')] \\ G_{zt}^{fs}(r,r') &= \mu_0/4\pi \cdot W^{fs}(r,r') \\ K_\phi^{fs}(r,r') &= 1/4\pi\varepsilon_s [T^{fs}(r,r') + Q^{fs}(r,r')] \\ P^{fs}(r,r') &= \mu_0/4\pi \cdot C^{fs}(r,r') \end{aligned} \tag{5}$$

where complex permittivity ϵ_s is given by $\epsilon_{s,r}\epsilon_0 - j\,\sigma_s/\omega$. In (5) $T^{fs}, U^{fs}, V^{fs}, W^{fs}, Q^{fs}$ and C^{fs} are defined with the generalized Sommerfeld integral $S_n^{fs}[f]$, as follows:

$$\begin{aligned} T^{fs}(r,r') &= S_0^{fs}[1/\gamma_s] \\ U^{fs}(r,r') &= S_0^{fs}[\Gamma_s^h/\gamma_s] \\ V^{fs}(r,r') &= S_0^{fs}[-\Gamma_s^e/\gamma_s] \\ W^{fs}(r,r') &= S_1^{fs}[(\Gamma_s^e - \Gamma_s^h)/\lambda^2] \\ C^{fs}(r,r') &= S_0^{fs}[(\Gamma_s^e - \Gamma_s^h)/\lambda^2] \\ Q^{fs}(r,r') &= S_0^{fs}[\Gamma_s^e/\gamma_s] - S_0^{fs}[(\Gamma_s^e - \Gamma_s^h)/\gamma_s\lambda^2]k_s^2 \end{aligned} \tag{6}$$

Note that all these items arise from the presence of the air-ground boundary in the space.

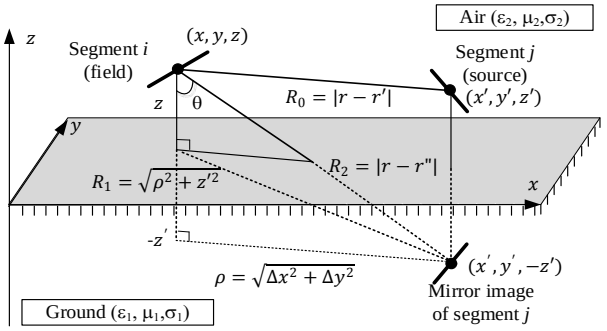

Fig. 1 Configuration of segments in the air-ground medium (r, r', and r" denote that locations of field, source, and its image points, respectively).

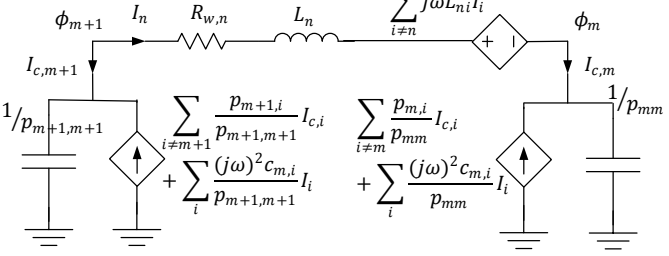

Fig. 2 Equivalent circuit of a line segment

With the geometric parameters of source and field points shown in Fig. 1, $S_n^{fs}[f]$ is expressed by

$$\begin{aligned} S_n^{fs}[f] &= \int_0^\infty f(\lambda) e^{-\gamma_s z' - \gamma_f z} J_n(\lambda\rho) \lambda^{n+1} d\lambda \\ &= 0.5 \int_{-\infty}^{+\infty} f(\lambda) e^{-\gamma_s z' - \gamma_f z} H_n^{(2)}(\lambda\rho) \lambda^{n+1} d\lambda \end{aligned} \tag{7}$$

where $\gamma_i = \sqrt{\lambda^2 - k_i^2}$ $(i = f, s)$, and real $(\gamma_i) \geq 0$. wavenumber $k_i = \omega\sqrt{\epsilon_i \mu_i}$. Both z' and z are the absolute values of the vertical coordinates of source and field points. Horizontal distance $\rho = \sqrt{\Delta x^2 + \Delta y^2}$. Both J_n and $H_n^{(2)}$ are respectively the Bessel function of the 1st kind and Hankel function of the 2nd kind at order *n*. For source and field points in the same layer, T^{fs} can be explicitly expressed, using the identity in (A2), by

$$\begin{aligned} T^{fs}(r, r') &= \int_0^\infty \gamma_s^{-1} e^{-\gamma_s |z'-z|} J_0(\lambda\rho)\lambda d\lambda \\ &= e^{-jk_s R_0} / R_0 \end{aligned} \tag{8}$$

where distance $R_0 = \sqrt{\rho^2 + (z'-z)^2}$, as illustrated in Fig. 1.

In the Sommerfeld integrals shown in (6), both Γ_s^e and Γ_s^h are the reflection coefficients of TE and TM mode waves in the Green's function transmission line [40-41], and are given by

$$\begin{aligned} \Gamma_s^e &= -(n_s\gamma_s - \gamma_{\bar{s}})(n_s\gamma_s + \gamma_{\bar{s}})^{-1} \\ \Gamma_s^h &= (\gamma_s - \gamma_{\bar{s}})(\gamma_s + \gamma_{\bar{s}})^{-1} \end{aligned} \tag{9}$$

where refractive index n_s is defined as $k_{\bar{s}}^2 / k_s^2$, and $\bar{s}$ denotes the non-source layer in the 2-layer medium. To facilitate an efficient computation of these SIs, the following parameters D_0, D_1 and D_2 are introduced to substitute Γ_s^e and Γ_s^h in the kernels,

$$\begin{aligned} D_0 &= \gamma_s^{-1} e^{-\gamma_s z' - \gamma_f z} \\ D_1 &= (\gamma_s - \gamma_{\bar{s}})(\gamma_s + \gamma_{\bar{s}})^{-1} \gamma_s^{-1} e^{-\gamma_s z' - \gamma_f z} \\ D_2 &= (\gamma_s - \gamma_{\bar{s}})(n_s\gamma_s + \gamma_{\bar{s}})^{-1} \gamma_s^{-1} k_s^2 e^{-\gamma_s z' - \gamma_f z} \end{aligned} \tag{10}$$

Sommerfeld integrals in (6) then are transformed into

$$\begin{aligned} T^{fs} &= \int_0^\infty D_0 J_0(\lambda\rho)\lambda d\lambda \\ U^{fs} &= \int_0^\infty D_1 J_0(\lambda\rho)\lambda d\lambda \\ V'^{fs} &= \int_0^\infty D_2 J_0(\lambda\rho)\lambda d\lambda \\ W^{fs} &= -2k_s^{-2} \int_0^\infty D_2 \gamma_s J_1(\lambda\rho)\lambda^2 d\lambda \\ C^{fs} &= -2k_s^{-2} \int_0^\infty D_2 \gamma_s J_0(\lambda\rho)\lambda d\lambda \end{aligned} \tag{11a}$$

and

$$\begin{aligned} V^{fs} &= -\kappa_s \cdot T^{fs} + (1-\kappa_s) \cdot V'^{fs} \\ Q^{fs} &= +\kappa_s \cdot T^{fs} + (1+\kappa_s) \cdot V'^{fs} \end{aligned} \tag{11b}$$

where κ_s is defined as $(1 - n_s)/(1 + n_s)$.

III. Integration of Sommerfeld Integrals

The Sommerfeld integrals in (11) are difficult to evaluate because of the singularity and slowly-decaying oscillation of the integrands. Different techniques have been proposed to integrate these integrands, including deforming the integration path for accelerating the convergence and avoiding the branch point.

In this section, a direct integration scheme along the real axis (DRXI) is adopted. Special functions are constructed to remove the singularity in these integrands by using the cancellation method, and to speed up the integration of the slowly-decaying integrands by removing low-order terms of their Taylor's series at $1/\lambda = 0$, as seen in Appendix A. The revised expressions of U^{fs} and V'^{fs} in (11) in the case of "Source in Air" are given as,

$$\begin{aligned} U^{fs} &= \int_0^\infty (D_1 + f_0^* - f_1^*) J_0(\lambda\rho)\lambda d\lambda - S_0^{fs}[f_0] + S_0^{fs}[f_1] \\ V'^{fs} &= \int_0^\infty (D_2 + f_0^* - f_1^*) J_0(\lambda\rho)\lambda d\lambda - S_0^{fs}[f_0] + S_0^{fs}[f_1] \end{aligned} \tag{12}$$

where $f_{0/1} = f_{0/1}^* e^{\gamma_s z' + \gamma_f z}$. Function f_0^* in (12) is employed to cancel out the singularity of the kernels in U^{fs} and V'^{fs}. Function f_1^* is added to cancel out low-order terms of the Talor's series of these kernels. In such a way, the revised kernels decline with $1/\lambda$ at the order of 3 or more when λ increases. f_1 can be obtained by examining the 1st and 2nd orders of the Talor's series of f_0 at $1/\lambda = 0$, and then are given by

$$\begin{aligned} f_0^*(\lambda) &= e^{-\gamma_s z' - k_{sf} z} \lambda_s^{-1} \\ f_1^*(\lambda) &= e^{-\lambda z' - k_{sf} z} \lambda^{-1} + 0.5 k_s^2 z' e^{-\gamma_b z' - k_{sf} z} (\lambda\gamma_b)^{-1} \end{aligned} \tag{13}$$

where $\gamma_b = (\lambda^2 + k_s^2)^{1/2}$ and $k_{sf} = (k_s^2 - k_f^2)^{1/2}$. The detail is given in Appendix A. With the identities in (A2), the corresponding SIs become

$$\begin{aligned} S_0^{fs}[f_0(\lambda)] &= e^{-jk_s R_1 - k_{sf} z} R_1^{-1} \\ S_0^{fs}[f_1(\lambda)] &= e^{-k_{sf} z'} (R_1^{-1} + 0.5 k_s^2 z' I_0[\Delta R_1^-] \cdot K_0[\Delta R_1^+]) \end{aligned} \tag{14}$$

where $\Delta R_1^{\pm} = 0.5jk_s(R_1 \pm z')$ and $R_1 = \sqrt{\rho^2 + z'^2}$, as illustrated in Fig. 1. Both I_n and K_n are respectively the modified Bessel functions of the 1st and 2nd kind at order 0. Expressions of other SIs are obtained similarly and are given in Appendix A.

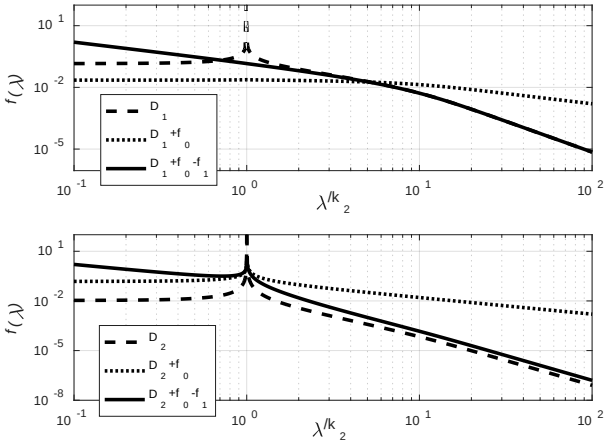

Fig. 3 Kernels of U^{22} and V'^{22} against λ normalized with k_2

Fig. 3 illustrates both the original and revised kernels of U^{22} and V'^{22} against λ normalized with k_2 at $z = z' = 0$. It is seen that a singularity is located at $\lambda = k_2$ in the original kernels D_1 and D_2. The singularity is removed by f_0 in the kernels $D_1 + f_0$ and $D_2 + f_0$. However, these kernels decay very slowly. By adding function f_1, the revised kernels finally decline with $1/\lambda$ at the order of 3.

In the case of "Source under Ground", SIs in (11) do not contain any singularity in the kernels. Special functions are just introduced to speed up the convergence only, so that the kernels decline with $1/\lambda$ at the order of 3. These functions and revised expressions of SIs are given in Appendix A.

IV. Quasi-static and Asymptotic Expressions of SIs

A. Quasi-static Expressions of SIs

Quasi-static expressions of Sommerfeld integrals are particularly interesting. They can be used to derive frequency-invariant PEEC models for fast time-domain simulation, in case that the distance of interest is much less than the wavelength of concern. In such a case, ω is considered to approach zero. By replacing γ_i ($i = s$ or f) with λ in (9), reflection coefficients Γ_s^e and Γ_s^h are simplified into

$$\Gamma_s^e \approx (1-n_s)(1+n_s)^{-1} = \kappa_s \qquad \Gamma_s^h \approx 0 \tag{15a}$$

The coefficient $(\Gamma_s^e - \Gamma_s^h)/\lambda^2$ can then be simplified into one of two expressions, as follows:

$$(\Gamma_s^e - \Gamma_s^h)/\lambda^2 \approx \begin{cases} \kappa_s/\lambda^2 \\ \kappa_s/\gamma_x\lambda \end{cases} \tag{15b}$$

The 2nd expression is obtained by replacing λ with γ_x where subscript x represents the layer in which the wave number has a larger absolute value, i.e., $|k_x| = \max\{|k_1|, |k_2|\}$. Note that the exponent $-\gamma_s z' - \gamma_f z$ in the SI turns to be $-\lambda(z'+z)$. With (15) and the identities in (A2), the quasi-static expressions of these integrals in (6) become

$$\begin{aligned} T_{qs}^{fs} &= \int_0^\infty e^{-\lambda(z'+z)} J_0(\lambda\rho)\, d\lambda = 1/R_2 \\ U_{qs}^{fs} &= \int_0^\infty 0 \cdot e^{-\lambda(z'+z)} J_0(\lambda\rho)\, d\lambda = 0 \\ V_{qs}^{fs} &= \int_0^\infty -\kappa_s \cdot e^{-\lambda(z'+z)} J_0(\lambda\rho)\, d\lambda = -\kappa_s/R_2 \\ W_{qs}^{fs} &= \int_0^\infty \kappa_s \cdot e^{-\lambda(z'+z)} J_1(\lambda\rho)\, d\lambda = m\kappa_s/R_2 \\ Q_{qs}^{fs} &= \int_0^\infty \kappa_s \cdot e^{-\lambda(z'+z)} J_0(\lambda\rho)\, d\lambda = \kappa_s/R_2 \end{aligned} \tag{16}$$

where $m = (R_2 - \Delta z)/\rho$ and $R_2 = \sqrt{\rho^2 + \Delta z^2}$, and $\Delta z = z + z'$.

To derive a closed-form quasi-static expression for C_{qs}^{fs}, the second expression of the coefficient in (15b) is adopted. By substituting this expression into (6) and replacing $-\gamma_s z' - \gamma_f z$ with $-\gamma_x(z'+z)$, the following expression is obtained,

$$\begin{aligned} C_{qs}^{fs} &\approx \kappa_s \int_0^\infty e^{-\gamma_x(z'+z)} J_n(\lambda\rho)/\gamma_x \, d\lambda \\ &\approx \kappa_s I_0[\Delta R_2^-] \cdot K_0[\Delta R_2^+] \\ &\approx \kappa_s K_0[\Delta R_2^+] \end{aligned} \tag{17}$$

with the identity given in (A4), where $\Delta R_2^\pm = 0.5jk_s(R_2 \pm \Delta z)$. It is noted in [37] that the contribution of C_{qs}^{fs} in a quasi-static PEEC model is very small, and can be neglected.

SIs in (16) except T_{qs}^{fs} are considered as the contribution from images of the source. They are located either at the source point or the mirror image point. The magnitude is equal to the source current or charge corrected with a factor of 0, $\pm\kappa_s$ or $m\kappa_s$. The entire space around a source image is filled up with the source medium. Thus, all the images have the same Green function, i.e., $1/R_2$, as seen in (16). Fig. 4 illustrates the configuration of horizontal and vertical current dipoles (I_u, I_v), charges (q_0) and their images contributing to the individual components of Green's functions. Four difference cases are presented according to the locations of the source and field points. Note that the image is located at the source point if both source and field points are in the different layers, or at its mirror image point if they are in the same layer. It is found that the horizontal current dipole does not have its image contribution to the horizontal vector potential ($G_{tt}^{fs} = 0$), but has the image contribution to the vertical vector potential G_{zt}^{fs}. Therefore, Green's functions in (5), subsequently the circuit parameters, can be viewed as those due to the source and/or its image.

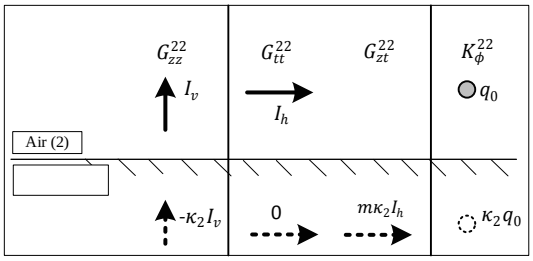

(a) Source and field pts. in the air

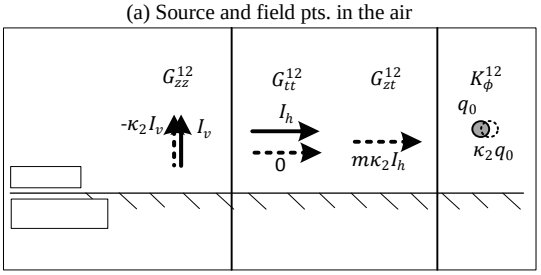

(b) Source pt. in the air and field pt. under the ground

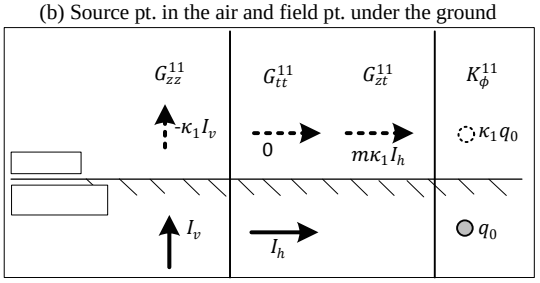

(c) Source and field pts. under the ground

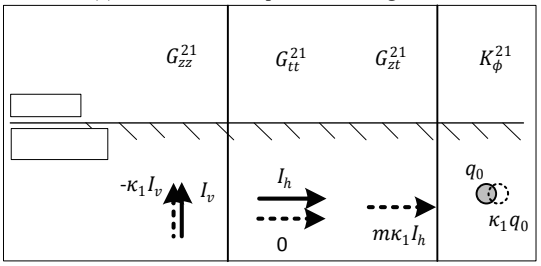

(d) Source pt. under the ground and field pt. in the air

Fig. 4 Sources and the images in the two-layer space: $m = (R_2 - \Delta z)/\rho$
(solid line = source, dash line = image,
I_v: vertical current dipole, I_h: horizontal current dipole)

Table 1 shows Green's functions for current and charge elements when the frequency approaches zero. Note that in this table $\kappa_1 = 1$ and $\kappa_2 = -1$. It is found that cross-boundary

Green's functions K_{ϕ}^{12} and G_{zz}^{21} are equal to zero due to cancellation. This indicates that there is no mutual electric or magnetic coupling between these elements. It is noted that these Green's functions do not vary with frequency. Circuit parameters can then be obtained efficiently.

Table 1 Green's functions for diff. source/image point (s) and field point (f) (note: coefficient $\mu_0/4\pi$ or $1/4\pi\epsilon_{1/0}$ in these functions is suppressed)

GF components	G_{zz}^{fs}	G_{tt}^{fs}	G_{zt}^{fs}	K_{ϕ}^{fs}
$s=f=2$ (air)	$1/R_0$+$1/R_2$	$1/R_0$	-m/R_2	$1/R_0$-$1/R_2$
$s=2, f=1$	$2/R_2$	$1/R_2$	-m/R_2	0
$s=f=1$ (ground)	$1/R_0$-$1/R_2$	$1/R_0$	m/R_2	$1/R_0$+$1/R_2$
$s=1, f=2$	0	$1/R_2$	m/R_2	$2/R_2$

B. Asymptotic expressions of SIs

For the case in which both source and field points are situated in the air, the asymptotic approximation of SIs in (6) is feasible. These expressions can be derived by using the steepest descent method [22-25]. Consider the integral of the type

$$I=\int_{\Gamma} F(\alpha)e^{\Omega\, q(\alpha)}d\alpha \tag{18}$$

The general idea is to find the steepest descent path Γ_{sd} passing through a saddle point, so that the integral in this path around the saddle point is significant. At the saddle point, the integrand reaches the maximum. The original integral can then be approximated by the integral along this new path [22], which has a closed-form expression.

For the source and field points in the air, the Sommerfeld integral can be transformed into the form shown in (18) according to Appendix B. It is expressed by

$$S_n^{22}[f(\lambda)]=\int_{\Gamma} f(k_2\sin\alpha)\frac{k_2\cos\alpha(k_2\sin\alpha)^n e^{j(1+2n)\pi/4}}{\sqrt{2\pi k_2 R_2\sin\theta\sin\alpha}} \cdot e^{-jk_2R_2\cos(\alpha-\theta)}d\alpha \tag{19}$$

where both parameters θ and α are defined by $\rho=R_2 sin\theta$ and $\lambda=k_2 sin\alpha$. Appendix B derives the general formula of the asymptotic expression of S_n^{22} in (19), as shown below

$$S_n^{22}[f]\approx e^{j(n+1)\pi/2}f(k_2\sin\theta)k_2\cos\theta(k_2\sin\theta)^n\frac{e^{-jk_2R_2}}{R_2} \tag{20}$$

(20) is valid when no singularity or branch point is intercepted in the deformation to the steepest descent path [19].

Note that the kernels of Sommerfeld integrals in (6) can be expressed with $\lambda=k_2 sin\theta$, as seen in (B7). The asymptotic expressions of these SIs then are simplified, as follows:

$$\begin{aligned}
U_{asym}^{22}&=\frac{\cos\theta-\sqrt{n_2-\sin^2\theta}}{\cos\theta+\sqrt{n_2-\sin^2\theta}}\cdot\frac{e^{-jk_2R_2}}{R_2}\\
V_{asym}^{22}&=\frac{n_2\cos\theta-\sqrt{n_2-\sin^2\theta}}{n_2\cos\theta+\sqrt{n_2-\sin^2\theta}}\cdot\frac{e^{-jk_2R_2}}{R_2}\\
W_{asym}^{22}&=\sin 2\theta\frac{\cos\theta-\sqrt{n_2-\sin^2\theta}}{n_2\cos\theta+\sqrt{n_2-\sin^2\theta}}\cdot\frac{e^{-jk_2R_2}}{R_2}\\
C_{asym}^{22}&=\frac{-j2\cos\theta}{k_2}\frac{\cos\theta-\sqrt{n_2-\sin^2\theta}}{n_2\cos\theta+\sqrt{n_2-\sin^2\theta}}\cdot\frac{e^{-jk_2R_2}}{R_2}\\
Q_{asym}^{22}&=\left(\frac{2\cos\theta}{n_2\cos\theta+\sqrt{n_2-\sin^2\theta}}-1\right)\cdot\frac{e^{-jk_2R_2}}{R_2}
\end{aligned} \tag{21}$$

V. Numerical Results

A) Numerical calculation of Green's functions

In the computation of the SIs in (11), the transformation technique [14] is adopted to relax the dense oscillation around the branch cut point. The shank transformation [20] is applied to accelerate the convergence of the integration in the semi-infinite region. In each region, λ is divided into small segments, and the integral in each segment is calculated by using the Gauss–Legendre quadrature rule [14,43].

We express the calculation results of SIs in the form of $Xe^{-jk_2R_2}/R_2$, where X is called the normalized SI coefficient. Fig. 5 shows the profiles of these SI coefficients, i.e., normalized U, V, W, Q, and C over the $R_1-\theta$ space with $z=1$ m at 1 MHz. $R_1=\sqrt{\rho^2+z'^2}$ is normalized with the wavelength. Two different cases for source and field points in different layers are presented: source point (1) in the air and (2) under the ground. The soil parameters are set to be $\epsilon_{1,r}=4\epsilon_0$ and $\sigma_1=0.01\ s$, and also are adopted for other calculations later.

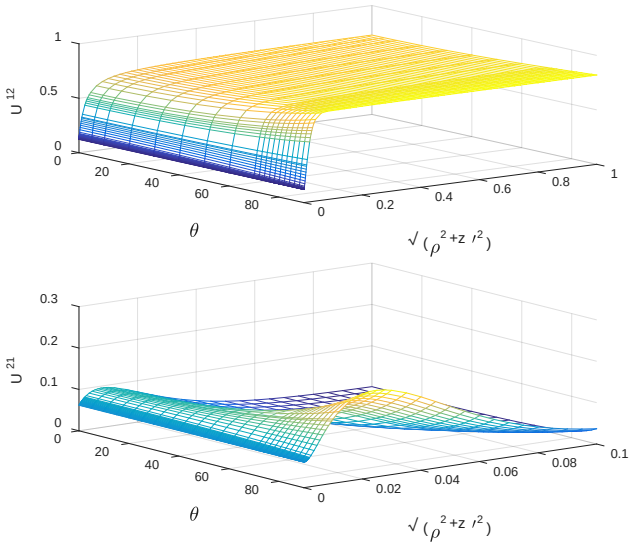

(a) U^{12} (source in the air) and U^{21} (source under the ground)

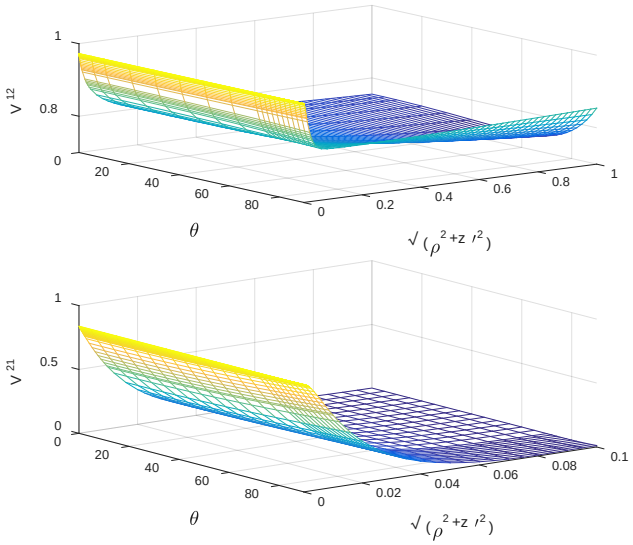

(b) V^{12} (source in the air) and V^{21} (source under the ground)

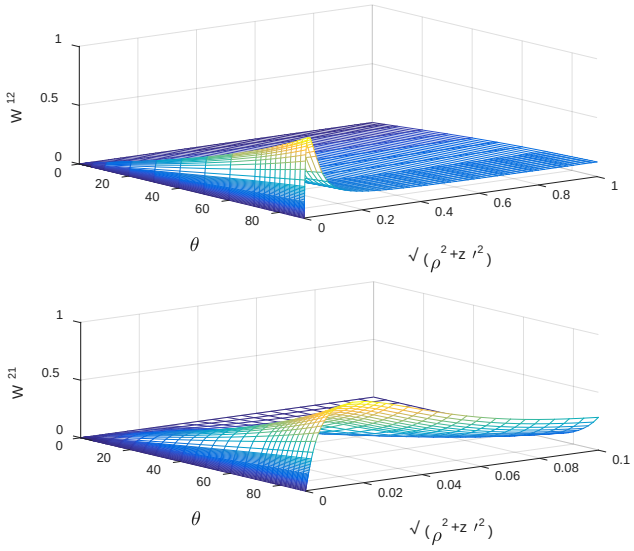

(c) W^{12} (source in the air) and W^{21} (source under the ground)

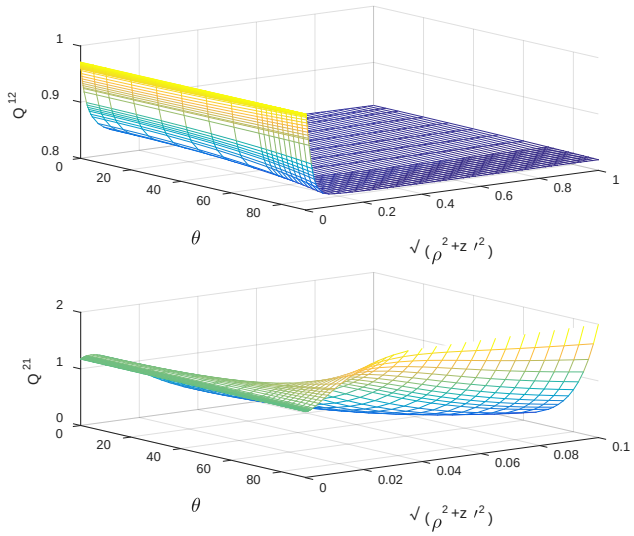

(d) Q^{12} (source in the air) and Q^{21} (source under the ground)

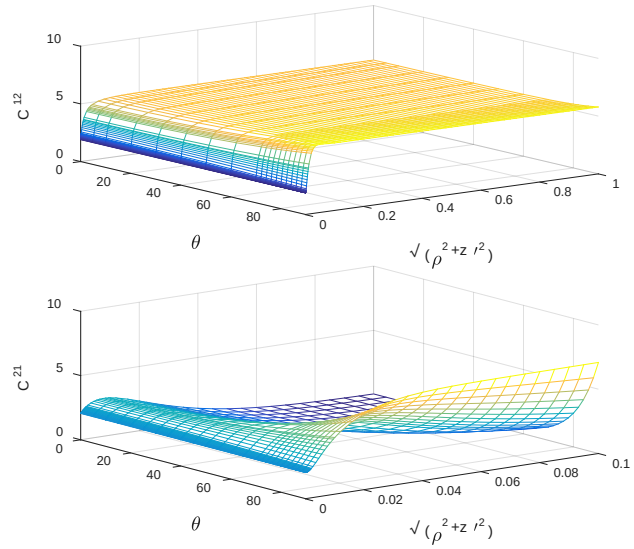

(e) C^{12} (source in the air) and C^{21} (source under the ground)

Fig. 5 Profiles of normalized coefficients for SIs in (11)

A comparison with the method using the Sommerfeld integral paths [16] has been made. Fig. 6 shows the calculated results using the proposed method and the calculation module adopted in NEC2. We varied the frequency from 100 Hz to 100

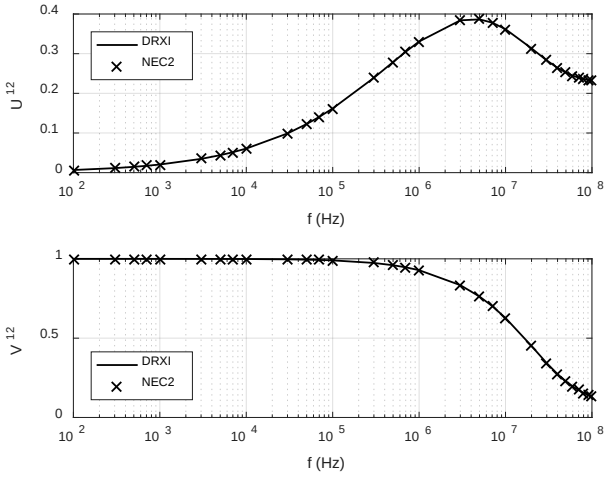

(a) U^{12} and V^{12}

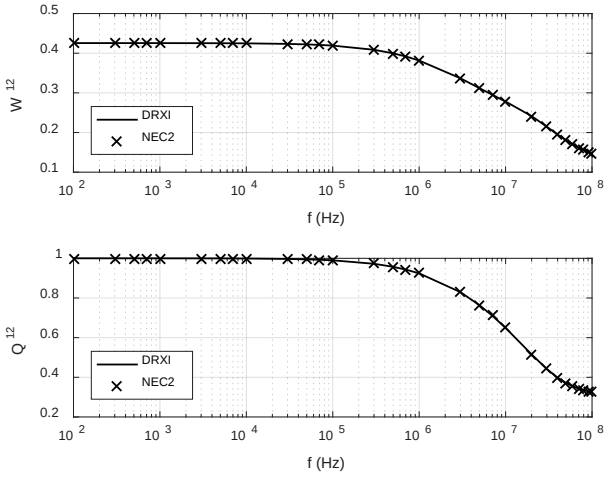

(b) W^{12} and Q^{12}

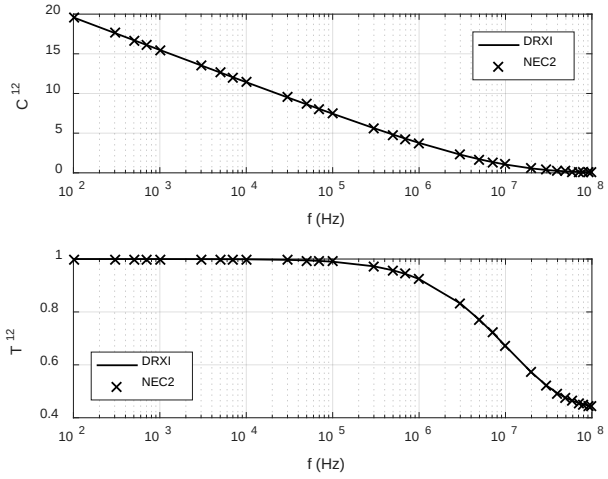

(c) C^{12} and T^{12}

Fig. 6 Comparison of normalized SI coefficients calculated with NEC2 and DRXI
(f = 1 MHz, $R_2 = 3\ m$, $z = 1\ m$, and $\theta = 30^0$)

MHz. The source point is fixed in the air with $R_2 = 3\ m$ and $\theta = 30^0$, and the field point is located under the ground with $z = 1\ m$. It is found that both results match well, and the average error over the whole frequency range is 0.1% or less. Computation time by these two methods also is compared. The computation time in a PC with an i7-7700 CPU for generating a lookup table of 25x61 entries is 7.63 sec with the NEC2 method, 2.27 sec with the proposed DRXI method.

A comparison with the quasi-static expressions of SIs in (6) also is made. Table 2 shows the magnitude of normalized SI coefficients calculated with (16-17) and the proposed DRXI method. Four different scenarios of source and field points are considered in the calculation. Those are (a) the source and field points in the air, (b) the source point in the air and field point under the ground, (c) the source and field points under the ground, and (d) the source point under the ground and field point in the air. In the calculation, the frequency was set to be 1 MHz, and both normalized distance R_2 and angle θ are respectively set to be $1e^{-7}$ and 45^o. If both source and field points are in different layers, the vertical distance z' is set to be zero. It is found in the table that these results match very well.

Table 2 Quasi-static values of normalized SI coefficients
(f =1 MHz, normalized $R_2 = 1e^{-7}$ and $\theta = 45^o$)

	U^{fs}	V^{fs}	W^{fs}	Q^{fs}	C^{fs}
(16-17)	0	0.9998	0.4141	0.9998	3.592e-4
(a)	3.826e-6	0.9998	0.4141	0.9998	3.725e-4
(b)	3.856e-6	0.9998	0.4141	0.9998	3.726e-4
(c)	1.475e-6	0.9997	0.4141	0.9998	3.668e-4
(d)	1.475e-6	0.9997	0.4141	0.9998	3.668e-4

Fig. 7 shows normalized coefficients of the SIs with large arguments, calculated by the proposed procedure and their asymptotic expressions in (21). In the numerical calculation, SIs are evaluated against angle θ at 1 MHz with normalized $R_0 = 10$. Both source and field points are located in the air. It is found that the results match very well for the angle θ greater than 15^o. For small angle θ, the steepest descent path will cross over the branch cut. The asymptotic approximation is not so accurate. This leads to a relatively large discrepancy between these results, particularly for Sommerfeld integrals V^{22} and C^{22}.

B) Simulation of transients with the Green's functions

In this section, an application of Green's functions for transient analysis in a simple circuit is presented. Fig. 8 shows the configuration of this circuit, which is made of two 2 m x 2 m square loops arranged in parallel. The loop in the air is excited by a lightning current impulse with a rising front of 0.25 μs. Both the current in the ground loop and the source voltage on the air loop are evaluated using the modified nodal analysis approach with the PEEC model [37].

In the simulation, all the wires are divided into a number of segments with a length of 0.1 m. Frequency-domain circuit parameters of these segments, such as *L*, *p*, and *c* are calculated first with (2) up to 25 MHz, using the lookup tables of SIs built with the proposed procedure. The solution is obtained in the frequency domain, and an inverse Fourier transform technique is applied to obtain the time-domain waveforms of both current and voltage. Fig. 9 shows both the transient current I_g (ground loop) and voltage V_a (air loop) in this circuit using the PEEC modeling approach. For comparison, simulation results obtained by the Finite-Difference Time-Domain (FDTD) method using a thin-wire model [44], which is applied to simulate a wire structure, also are presented. It is found that both results match well with a difference of less than 1%.

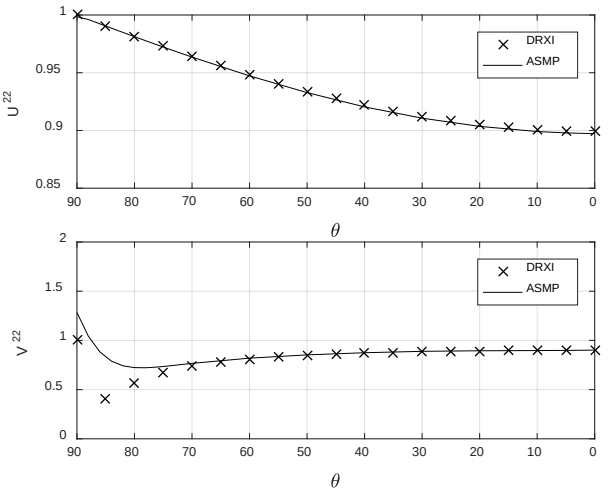

(a) U^{22} and V^{22}

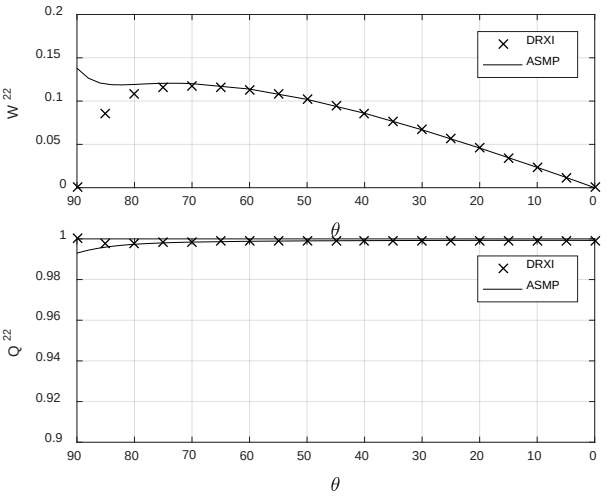

(b) W^{22} and Q^{22}

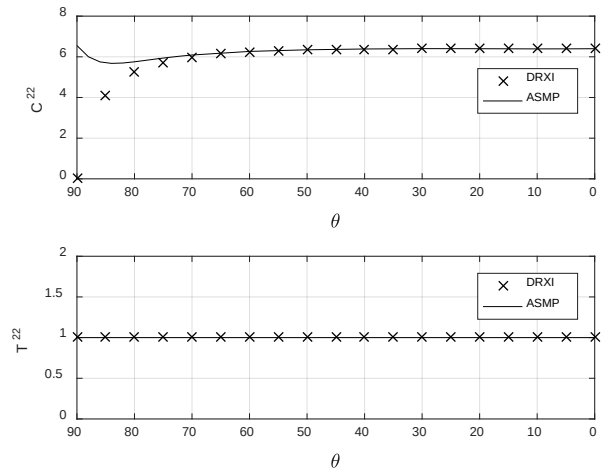

(c) C^{22} and T^{22}

Fig. 7 Comparison of SI coefficients calculated with asymptotic expressions and DRXI under large arguments (f = 1 MHz, and normalized $R_2 = 10$)

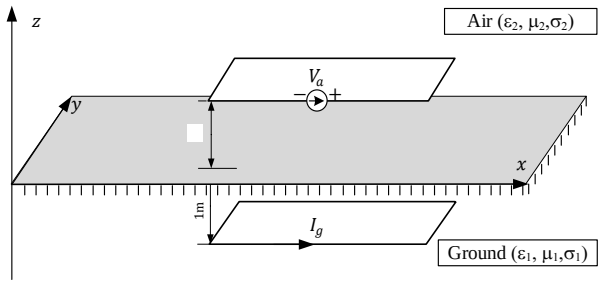

Fig. 8. Configuration of a testing system with two parallel square loops

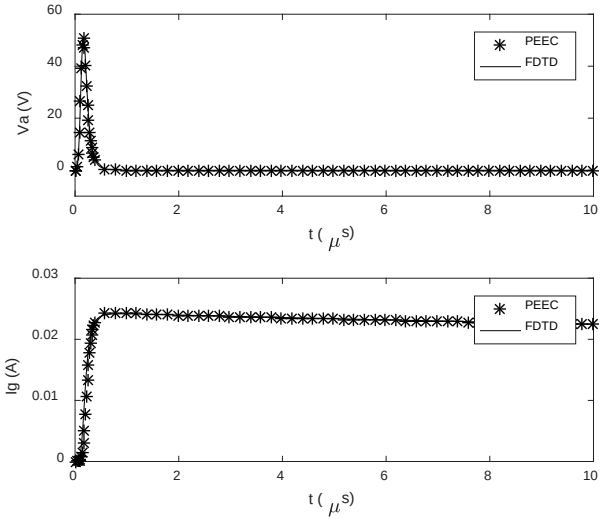

Fig. 9 Source loop voltage and ground loop current calculated with the PEEC and FDTD methods

VI. Conclusions

This paper presented a numerical evaluation of Green's functions for both vector and scalar potentials used in the PEEC formulation in the air-lossy ground space. Both source and field points can be located in any of these two layers. These Green's functions are expressed with generalized Sommerfeld integrals. The robust direct real-axis integration approach was presented with the techniques for singularity subtraction and convergence acceleration. A complete set of formulas was available to facilitate the easy generation of computer codes. Closed-form expressions were derived for the quasi-static and asymptotic approximation of SIs. Comparisons have been made with NEC2 and those approximate expressions, and good agreements were observed.

The image model was developed for quasi-static Green's functions. An image is located at the source point if both source and field points are in the different layers, or at its mirror image point if they are in the same layer. The entire space around a source image is filled up with the source medium. Therefore, Green's functions can be considered to be contributed by the source and/or its image in the space filled up with the source medium. It is found that the horizontal current dipole does not have its image contribution to the horizontal vector potential, but has the image contribution to the vertical vector potential. At low frequency, the vertical current dipole under the ground does not have any cross-boundary contribution to the vertical vector potential but has a double contribution when it is located in the air. A similar pattern also is observed for the point charge. This image model can be used to derive the quasi-static PEEC model of the wires in the air/lossy ground space, similar to those presented in [36-37]. This will help to achieve fast simulation of lightning transients, as the circuit parameters are frequency independent and a time-domain solution procedure can be adopted. The proposed numerical procedure can be applied to generate lookup tables of SIs, which are indispensable in the evaluation of PEEC parameters of a large number of wire segments in the air and/or ground.

Acknowledgment

The work leading to this paper was supported by grants from the RGC of the HKSAR (Project No. 15210018 and 15208019) and the Research Committee of HK PolyU.

References

[1] A.E. Ruehli, G. Antonini, and L. Jiang, Circuit oriented electromagnetic modeling using the PEEC techniques, John Wiley & Sons, Inc. New Jersey, 2017

[2] J. Nitsch, F. Gronwald, G. Wollenberg, Radiating nonuniform transmission-line systems, John Wiley & Sons, Inc., New Jersey, 2009

[3] A.E. Ruehli, "Equivalent circuit models for three-dimensional multi-conductor systems," IEEE Trans. on MTT, vol. 22, no. 3, 1974, pp. 216-221.

[4] G. Antonini, S. Cristina and A. Orlandi, "PEEC modeling of lightning protection systems and coupling to coaxial cables," IEEE, Trans. on EMC, vol. 40 no. 4, 1998, pp481

[5] A. Orlandi and F. Schietroma F, "Attenuation by lightning protection system of induced voltages due to direct strikes to a building," IEEE Trans. on EMC, vol. 8 no. 1, 1996, pp. 43-50

[6] P. Yutthagowith, A. Ametani, N. Nagaoka and Y. Baba, "Application of the partial element equivalent circuit method to analysis of transient potential rises in grounding systems," IEEE Trans. on EMC, vol. 53 no. 3, 2011, pp726-736

[7] H. Chen, Y. Du and M. Chen, "Lightning transient analysis of radio base stations." IEEE Trans on PWRD, Vol. 33, no. 5, 2018, pp. 2187-2197

[8] Ruihan Qi, Y. Du and Mingli Chen, "Lightning-generated transients in buildings with an efficient PEEC method," IEEE Trans. on Magnetics, vol. 55, no. 1, 2019, pp. 1-5.

[9] Ruihan Qi, Y. Du and Mingli Chen, "Time-domain PEEC transient analysis for a wire structure above the perfectly conducting ground with the incident field from a distant lightning channel," IEEE Trans. on EMC, DOI: 10.1109/TEMC.2019.2925140

[10] Yang Zhang et al., "Lightning transient analysis of main and sub-main circuits in commercial buildings using PEEC method," IEEE Trans. on IA, vol. 56 no. 1 Jan-Feb. 2020, pp. 106-116

[11] Y. Zhang, H. Chen, Y. Du, "Lightning protection design of solar photovoltaic systems: Methodology and guidelines," EPSR, Vol. 174, 2019, Paper No. 105877

[12] J.R. Mosig and K.A. Michalski, "Sommerfeld integrals and their relation to the development of planar microwave devices," IEEE Journal of Microwaves, vol. 1, no. 1, 2021, pp. 470-480.l

[13] M. Siegel and R.W.P. King, "Electromagnetic fields in a dissipative half-space, a numerical approach," J. Appl. Phys., vol. 134, no. 6, 1970, pp. 2415-2423.

[14] W.A. Johnson and D.G. Dudley, "Real axis integration of Sommerfeld integrals: source and observation points in air," Radio Science, vol. 18, pp. 175-186, 1983

[15] Z.H. Firouzch and G.A.E. Vandenbosch, "Efficient evaluation of Green's functions for lossy half-space problems," PIER, vol. 109, pp. 139-157, 2010

[16] R.J. Lytle and D.L. Lager, UCRL-51688: Numerical evaluation of Sommerfeld integrals, Lawrence Livermore Laboratory, Oct. 23, 1974

[17] K.A. Michalski and J.R. Mosig, "The Sommerfeld half-space problem revisited: from radio frequencies and Zenneck waves to visible light and Fano modes," Journal of Electromagnetic Waves and Applications, vol. 30, no. 1,2016, pp. 1-42

[18] G.J. Burke et al., Numerical Electromagnetic Code (NEC), Technical document 116, Naval Ocean Systems Center, San Diego, 1980.

[19] J.R. Mosig and A.G. Melcon, “Green’s functions in lossy layered media: integration- along the imaginary axis and asymptotic behavior,” IEEE Trans. on AP, vol. 51, no. 1, 2003, pp. 3200 – 3208.
[20] K.A. Michalski, “Extrapolation methods for Sommmerfeld integral trails,” IEEE Trans. on AP, vol. 46, no. 10, 1998, pp. 1405-1418
[21] R. Golubovic, A.G. Polimeridis and J.R. Mosig, “Efficient algorithms for computing Sommerfeld integral tails,” IEEE Trans. on AP, vol. 60, no. 5, 2012, pp. 2409-2417
[22] P. Parhami, Y. Rahmat-Samii, and R. Mittra, “An efficient approach for evaluating Sommerfeld integrals encountered in the problem of a current element radiating over lossy ground,” IEEE Trans. on AP, vol. 28, no. 1, 1980, pp. 100-11-4
[23] K.A. Michalski, “On the efficient evaluation of integrals easing in the Sommerfeld half-space problem,” IEE Proces. vol. 132, Pt. H. no. 5, 1985, pp. 312-318
[24] Y. Rahmat-Samii, R. Mittra and P. Parhami, “Evaluation of Sommerfeld integrals for lossy half-space problems,” Electromagnetics, Vol. 1 Pt. 1, 1981, pp.1-28.
[25] A. Hochman and Y. Leviatan, “A numerical methodology for efficient evaluation of 2D Sommerfeld integrals in the dielectric half-space problem,” IEEE Trans. On AP, vo. 58, no. 2, Feb. 2010, pp. 413-431.
[26] Y. L. Chow, J. J. Yang, D. G. Fang and G. E. Howard, "A closed-form spatial Green's function for the thick microstrip substrate", IEEE Trans. on MTT., vol. 39, no. 3, pp. 588-592, Mar. 1991.
[27] M. I. Aksun, "A robust approach for the derivation of closed-form Green's functions", IEEE Trans. MTT., vol. 44, no. 5, pp. 651-658, May 1996.
[28] Y Liu, LW Li, TS Yeo and MS Leong, “Application of DCIM to MPIE-MoM analysis of 3D PEC objects in multilayered media,” IEEE Trans. on AP, vol. 50, no. 2, 2002, pp. 157-162
[29] F. Ling and J.-M. Jin, "Discrete complex image method for Green's functions of general multilayer media", IEEE Microw. Guided Wave Lett., vol. 10, no. 10, pp. 400-402, Oct. 2000.
[30] M. I. Aksun and G. Dural, "Clarification of issues on the closed-form Green's functions in stratified media", IEEE Trans. on AP., vol. 53, pp. 3644-3653, Nov. 2005.
[31] M. Yuan, T. K. Sarkar and M. Salazar-Palma, "A direct discrete complex image method from the closed-form Green's functions in multi-layered media", IEEE Trans. MTT., vol. 54 Mar. 2006, pp. 1025-1032
[32] M. Yuan et al. “Two-dimensional discrete complex image method (DCIM) for closed-form Green’s function of arbitrary 3D structures in general multilayered media,” IEEE Trans. on AP, vol. 56 no. 5, 2008, pp. 1350-1357.
[33] Ergun Simsek, Qing Huo Liu and Baojun Wei, “Singularity subtraction for evaluation of Green’s functions for multilayer media,” IEEE Trans. on MTT, vol. 54, no.1 Jan. 2006, pp. 216-225
[34] A. Alparslan, M.I. Aksun and K.A. Michalski, “Closed-form Green’s functions in planar layered media for all ranges and materials,” IEEE Trans. on MTT, vol. 58, no. 3, 2010, pp. 602-613
[35] F. Mesa, R.R. Boix and F. Medina, “Closed-form expressions of multilayered planar Green’s functions that account for the continuous spectrum in the far field,” IEEE Tran. on MTT, vol. 56, no. 7, 2008, pp.1601-1614
[36] Y. Du, Xinhua Wang and Mingli Chen, “Circuit parameters of the vertical wires above the lossy ground in PEEC models,” IEEE Trans on EMC vol. 53 no. 4, 2012, pp871-879
[37] Ruihan Qi, Y. Du and Mingli Chen, “A full-wave PEEC model of thin-wire structures above the lossy ground," DOI 10.1109/TEMC.2019.2949346
[38] K. A. Michalski and D. Zhang, “Electromagnetic scattering and radiation by surfaces of arbitrary shape in layered media, part I: theory,” IEEE Trans. on AP, vol. 38 no. 3, 1990, pp. 335-344.
[39] S.V. Kochetov, M. Leone and G. Wollenberg, “PEEC formulation based on dyadic Green’s functions for layered media in the time and frequency domains,” IEEE Trans. on EMC, Vol. 50, No. 4, Feb. 2008, pp. 953-963.
[40] R. Qi, The improved PEEC method for grounded structures above lossy ground for lightning analysis, Ph.D thesis, The Hong Kong Polytechnic University, 2019
[41] K.A. Michalski and J.R. Mosig, “Multilayered media Green’s functions in integral equation formulations,” *IEEE Trans. on AP*, vol. 45, no. 3, pp. 508-519, 1997
[42] I.S. Gradshteyn and I.M. Ryzhik, Table of Integrals, Series, and Products: Formulas 6.6.11, 6.637(1), Academic Press, New York, 2007
[43] GJ Burke and A.J. Poggio, Numerical electromagnetic code (NEC) – method of the moment – Part II: program description – code (EVLUA module), Report UCID-18834, Lawrence Livermore Laboratory, 1981.
[44] Y. Du and Binghao Li and Mingli Chen, "The extended thin wire model of lossy round wire structures for FDTD simulations," IEEE Trans. on PWRD, Vol. 32, no. 2, pp. 2472-2480, 2017

Appendix A

The singularity in an integrand can be removed by a cancellation method with a specific function, the Sommerfeld integral of which has a closed-form expression. Let the special function $f_0^*(\lambda)$ be $e^{-\gamma_s z' - k_{sf} z}/\gamma_s$, where $k_{sf} = (k_s^2 - k_f^2)^{1/2}$. The revised kernels of T^{fs}, U^{fs} and V'^{fs} in (11), when λ approaches k_s, become

$$\begin{aligned}
\lim_{\lambda\to k_s}[D_0 - f_0^*] &= \lim_{\lambda\to k_s}\frac{1}{\gamma_s}[1-1]e^{-k_{sf}z'} = 0 \\
\lim_{\lambda\to k_s}[D_1 + f_0^*] &= \lim_{\lambda\to k_s}\frac{1}{\gamma_s}[\frac{\gamma_s-\gamma_{\bar{s}}}{\gamma_s+\gamma_{\bar{s}}}+1]e^{-k_{sf}z'} \\
&= 2(\gamma_s+\gamma_{\bar{s}})e^{-k_{sf}z'} \qquad \text{(A1)} \\
\lim_{\lambda\to k_s}[D_2 + f_0^*] &= \lim_{\lambda\to k_s}\frac{1}{\gamma_s}[\frac{(\gamma_s-\gamma_{\bar{s}})}{n_s\gamma_s+\gamma_{\bar{s}}}+1]e^{-k_{sf}z'} \\
&= (1+n_s)(n_s\gamma_s+\gamma_{\bar{s}})^{-1}e^{-k_{sf}z'}
\end{aligned}$$

The real-axis singularity of the revised kernels then disappears. Note that other kernels of W^{fs}, Q^{fs} and S^{fs} do not contain any real-axis singularity.

The Sommerfeld integral of $f_0^*(\lambda)$ can be expressed in a close form. Note that the following identities hold [42],

$$\begin{aligned}
&\int_0^\infty \frac{e^{-\sqrt{\lambda^2+k_s^{*2}}z^*}}{\sqrt{\lambda^2+k_s^{*2}}}J_0(\lambda\rho)\lambda d\lambda = e^{-jk_s^*R^*}/R^* \\
&\int_0^\infty \frac{e^{-\sqrt{\lambda^2+k_s^{*2}}z^*}}{\sqrt{\lambda^2+k_s^{*2}}}J_n(\lambda\rho)d\lambda = I_{n/2}[\Delta R^{*-}]K_{n/2}[\Delta R^{*+}] \qquad \text{(A2)} \\
&\int_0^\infty e^{-\lambda z^*}J_n(\lambda\rho)d\lambda = \begin{cases} 1/R^* & n=0 \\ (R^*-z^*)/\rho R^* & n=1 \end{cases}
\end{aligned}$$

where $R^* = \sqrt{\rho^2+z^{*2}}$, and z^* can be either z' or $z+z'$. $\Delta R^{*\pm} = 0.5k_s^*(R^* \pm z^*)$, and k_s^* can be either k_s or jk_s, With (A2), the Sommerfeld integral of $f_0^*(\lambda)$ is derived to be

$$\begin{aligned}
S_0^{fs}[f_0(\lambda)] &= \int_0^\infty \gamma_s^{-1}e^{-\gamma_s z' - \gamma_{sf} z}J_0(\lambda\rho)\lambda d\lambda \\
&= e^{-jk_sR_1 - k_{sf}z}/R_1 \qquad \text{(A3)}
\end{aligned}$$

where $f_0 = f_0^* e^{\gamma_s z' + \gamma_f z}$, and $R_1 = \sqrt{\rho^2+z'^2}$.

It is noted that the Sommerfeld integrals converge slowly with increasing λ. To accelerate the convergence at large argument λ, we expand the elements of these modified kernels in (9) with a Taylor series at $1/\lambda = 0$, as follows:

$$
\begin{aligned}
f_0^* &= e^{-\gamma_s z' - k_{sf} z}\gamma_s^{-1} \\
&= e^{-\lambda z' - k_{sf} z}[\lambda^{-1} + 0.5k_s^2 z'\lambda^{-2}] + O(\lambda^{-3}) \\
D_0 &= e^{-\gamma_s z' - \gamma_f z}\gamma_s^{-1} \\
&= e^{-\lambda(z'+z)}[\lambda^{-1} + 0.5(k_s^2 z' + k_f^2 z)\lambda^{-2}] + O(\lambda^{-3}) \\
D_1 &= (\gamma_s - \gamma_{\bar{s}})(\gamma_s + \gamma_{\bar{s}})^{-1}\gamma_s^{-1} e^{-\gamma_s z' - \gamma_f z} \\
&= O(\lambda^{-3}) \\
D_2 &= (\gamma_s - \gamma_{\bar{s}})(n_s^2\gamma_s + \gamma_{\bar{s}})^{-1}\gamma_s^{-1} k_s^2 e^{-\gamma_s z' - \gamma_f z} \\
&= O(\lambda^{-3}) \\
D_2\gamma_s &= (\gamma_s - \gamma_{\bar{s}})(n_s\gamma_s + \gamma_{\bar{s}})^{-1} k_s^2 e^{-\gamma_s z' - \gamma_f z} \\
&= 0.5k_s^2\kappa_s e^{-\lambda(z'+z)}[\lambda^{-2} + 0.5(k_s^2 z' + k_f^2 z)\lambda^{-3}] + O(\lambda^{-4})
\end{aligned}
\tag{A4}
$$

In deriving the expressions in (A4), the following identities are used,

$$
\begin{aligned}
&\gamma_s^{-1} = \lambda^{-1} + O(\lambda^{-3}) \\
&e^{-\gamma_s z'} = e^{-\lambda z'}(1 + 0.5k_s^2 z'\lambda^{-2}) + O(\lambda^{-2}) \\
&(\gamma_s - \gamma_{\bar{s}})(\gamma_s + \gamma_{\bar{s}})^{-1} = 0.25(k_f^2 - k_s^2)\lambda^{-2} + O(\lambda^{-4}) \\
&(\gamma_s - \gamma_{\bar{s}})(n_s\gamma_s + \gamma_{\bar{s}})^{-1} = 0.5k_s^2\kappa_s\lambda^{-2} + O(\lambda^{-4})
\end{aligned}
\tag{A5}
$$

To speed up the computation, we construct additional functions f_1^*, f_2^*, f_3^* and f_4^* for f_0^*, D_0 and $D_2\gamma_s$. Those items in (A4), which decline with $1/\lambda$ at the order of less than 3 when λ increases, can then be canceled out by these functions at large λ. These introduced functions are given by

$$
\begin{aligned}
f_1^*(\lambda) &= e^{-\lambda z' - k_{sf} z}\lambda^{-1} + 0.5k_s^2 z' e^{-\gamma_b z' - k_{sf} z}(\lambda\gamma_b)^{-1} \\
f_2^*(\lambda) &= e^{-\lambda(z'+z)}\lambda^{-1} + 0.5(k_s^2 z' + k_f^2 z)e^{-\gamma_b(z'+z)}(\lambda\gamma_b)^{-1} \\
f_3^*(\lambda) &= 0.5k_s^2\kappa_s[e^{-\lambda(z'+z)} + 0.5(k_s^2 z' + k_f^2 z)e^{-\gamma_b(z'+z)}\gamma_b^{-1}]\lambda^{-2} \\
f_4^*(\lambda) &= 0.5k_s^2\kappa_s e^{-\gamma_b(z'+z)}(\lambda\gamma_b)^{-1}
\end{aligned}
\tag{A6}
$$

where $\gamma_b = (\lambda^2 + k_s^2)^{1/2}$. SIs in (11) are revised to be

$$
\begin{aligned}
T^{fs} &= \int_0^\infty (D_0 - f_0^* + f_1^* - f_2^*)J_0(\lambda\rho)\lambda d\lambda \\
&\quad + S_0^{fs}[f_0] - S_0^{fs}[f_1] + S_0^{fs}[f_2] \\
U^{fs} &= \int_0^\infty (D_1 + f_0^* - f_1^*)J_0(\lambda\rho)\lambda d\lambda - S_0^{fs}[f_0] + S_0^{fs}[f_1] \\
V'^{fs} &= \int_0^\infty (D_2 + f_0^* - f_1^*)J_0(\lambda\rho)\lambda d\lambda - S_0^{fs}[f_0] + S_0^{fs}[f_1] \\
W^{fs} &= -2k_s^{-2}\int_0^\infty (D_2\gamma_s + f_3^*)J_1(\lambda\rho)\lambda^2 d\lambda + 2k_s^{-2}S_1^{fs}[f_3] \\
C^{fs} &= -2k_s^{-2}\int_0^\infty (D_2\gamma_s + f_4^*)J_0(\lambda\rho)\lambda d\lambda + 2k_s^{-2}S_0^{fs}[f_4]
\end{aligned}
\tag{A7a}
$$

for the case of "Source in Air", and

$$
\begin{aligned}
T^{fs} &= \int_0^\infty (D_0 - f_0^*)J_0(\lambda\rho)\lambda d\lambda + S_0^{fs}[f_0] \\
W^{fs} &= -2k_s^{-2}\int_0^\infty (D_2\gamma_s + f_3^*)J_1(\lambda\rho)\lambda^2 d\lambda + 2k_s^{-2}S_1^{fs}[f_3] \\
C^{fs} &= -2k_s^{-2}\int_0^\infty (D_2\gamma_s + f_4^*)J_0(\lambda\rho)\lambda d\lambda + 2k_s^{-2}S_0^{fs}[f_4]
\end{aligned}
\tag{22}
$$

for the case of "Source under Ground", where $f_i = f_i^* e^{\gamma_s z' + \gamma_f z}$ and $i = 1, \ldots 4$. Note that there is no special function introduced for U and V' as their kernels have a decaying rate of the 3rd degree already. The SIs of these functions are expressed analytically as

$$
\begin{aligned}
S_0^{fs}[f_1(\lambda)] &= e^{-k_{sf} z'}[R_1^{-1} + 0.5k_s^2 z' I_0[\Delta R_1^-]\cdot K_0[\Delta R_1^+]] \\
S_0^{fs}[f_2(\lambda)] &= R_2^{-1} + 0.5(k_s^2 z' + k_f^2 z)I_0[\Delta R_2^-]\cdot K_0[\Delta R_2^+] \\
S_1^{fs}[f_3(\lambda)] &= 0.5k_s^2\kappa_s[(R_2 - \Delta z)\rho^{-1}R_2^{-1} + \\
&\qquad 0.5(k_s^2 z' + k_f^2 z)I_{1/2}[\Delta R_2^-]\cdot K_{1/2}[\Delta R_2^+] \\
S_0^{fs}[f_4(\lambda)] &= 0.5k_s^2\kappa_s I_0[\Delta R_2^-]\cdot K_0[\Delta R_2^+]
\end{aligned}
\tag{23}
$$

where $\Delta R_1^\pm = 0.5jk_s(R_1 \pm z')$, $\Delta R_2^\pm = 0.5jk_s(R_2 \pm \Delta z)$ and $\Delta z = z' + z$.

Appendix B

It is noted that under radiated conditions or large arguments ($k_2 r \gg 1$) in the air, Hankel functions in (7) can be approximated, as follows:

$$
\begin{aligned}
H_0^{(2)}(\lambda\rho) &\approx \sqrt{\frac{2}{\pi\lambda\rho}}e^{-j(\lambda\rho - \frac{1}{4}\pi)} \\
H_1^{(2)}(\lambda\rho) &\approx \sqrt{\frac{2}{\pi\lambda\rho}}e^{-j(\lambda\rho - \frac{3}{4}\pi)}
\end{aligned}
\tag{B1}
$$

The generalized Sommerfeld integral in (7) then is given by

$$
S_n^{22}[f] = \int_{-\infty}^{+\infty}\sqrt{\frac{1}{2\pi\rho}}f(\lambda)\lambda^{n+\frac{1}{2}}e^{-\gamma_2(z'+z)}e^{-j(\lambda\rho - \frac{n}{2}\pi - \frac{1}{4}\pi)}d\lambda \tag{B2}
$$

Introduce two parameters θ and α respectively for spectral-domain variables and temporal variables such that

$$
\begin{aligned}
\rho &= R_2\sin\theta \\
\lambda &= k_2\sin\alpha
\end{aligned}
\tag{B3}
$$

Then the following is obtained

$$
\begin{aligned}
z' + z &= R_2\cos\theta \\
\gamma_2 &= jk_2\cos\alpha \\
\gamma_1 &= jk_2\sqrt{n_2 - \sin^2\alpha}
\end{aligned}
\tag{B4}
$$

Thus, the Sommerfeld integral in (B2) can be written into

$$
\begin{aligned}
S_n^{22}[f(\lambda)] = \int_\Gamma & f(k_2\sin\alpha)\frac{k_2\cos\alpha(k_2\sin\alpha)^n e^{j(1+2n)\pi/4}}{\sqrt{2\pi k_2 R_2\sin\theta\sin\alpha}} \\
& \cdot e^{-jk_2R_2\cos(\alpha-\theta)}d\alpha
\end{aligned}
\tag{B5}
$$

Therefore, by comparing (18) with (B5), we obtain

$$
\begin{aligned}
\Omega &= k_2 R_2 \\
q(\alpha) &= -jk_2 R_2\cos(\alpha - \theta) \\
F(\alpha) &= f(k_2\sin\alpha)\frac{k_2\cos\alpha(k_2\sin\alpha)^n e^{j(1+2n)\pi/4}}{\sqrt{2\pi k_2 R_2\sin\theta\sin\alpha}}
\end{aligned}
\tag{B6}
$$

The saddle point α_s is obtained by letting $dq(\alpha)/d\alpha = 0$, i.e., $\alpha_s = \theta$ [22]. The steepest descent path is selected by letting the imaginary part of $q(\alpha)$ be one, i.e. $Re[\cos(\alpha - \theta)] = 1$, or $\cos(\alpha - \theta) = 1 - jt^2$ where parameter t varies from $-\infty$ to $+\infty$. According to [22], the integral of (B5) can be approximated by the integral along the steepest descent path

Γ_{sd}. Considering the slowing variation $F(\alpha)$ with t on Γ_{sd}, the following expression is obtained,

$$\begin{aligned} S_n^{22}[f] &\approx \sqrt{\frac{2\pi}{k_2 R_2}} F(\theta) e^{-j(k_2 R_2 - \frac{\pi}{4})} \\ &\approx e^{j(n+1)\pi/2} f(k_2 \sin\theta) k_2 \cos\theta (k_2 \sin\theta)^n \frac{e^{-jk_2 R_2}}{R_2} \end{aligned} \tag{B7}$$

where $f(*)$ in (B7) is the kernel of the corresponding Sommerfeld integral in (6). Note that the parameters of Sommerfeld integrals in (6) can be expressed, with $\lambda = k_2 sin\theta$, by

$$\begin{aligned} \frac{\Gamma_2^h}{\gamma_2} &= \frac{1}{jk_2 \cos\theta} \cdot \frac{\cos\theta - \sqrt{n_2 - \sin^2\theta}}{\cos\theta + \sqrt{n_2 - \sin^2\theta}} \\ \frac{\Gamma_2^e}{\gamma_2} &= \frac{-1}{jk_2 \cos\theta} \cdot \frac{n_2 \cos\theta - \sqrt{n_2 - \sin^2\theta}}{n_2 \cos\theta + \sqrt{n_2 - \sin^2\theta}} \\ \frac{\Gamma_s^e - \Gamma_s^h}{\gamma_2} &= \frac{-2}{k_2^2} \cdot \frac{\cos\theta - \sqrt{n_2 - \sin^2\theta}}{n_2 \cos\theta + \sqrt{n_2 - \sin^2\theta}} \end{aligned} \tag{B8}$$

Substituting (B8) into (B7) yields the asymptotic expressions of these SIs, as follows:

$$\begin{aligned} U_{asym}^{22} &= \frac{\cos\theta - \sqrt{n_2 - \sin^2\theta}}{\cos\theta + \sqrt{n_2 - \sin^2\theta}} \cdot \frac{e^{-jk_2 R_2}}{R_2} \\ V_{asym}^{22} &= \frac{n_2 \cos\theta - \sqrt{n_2 - \sin^2\theta}}{n_2 \cos\theta + \sqrt{n_2 - \sin^2\theta}} \cdot \frac{e^{-jk_2 R_2}}{R_2} \\ W_{asym}^{22} &= \sin 2\theta \frac{\cos\theta - \sqrt{n_2 - \sin^2\theta}}{n_2 \cos\theta + \sqrt{n_2 - \sin^2\theta}} \cdot \frac{e^{-jk_2 R_2}}{R_2} \\ C_{asym}^{22} &= \frac{-j2\cos\theta}{k_2} \frac{\cos\theta - \sqrt{n_2 - \sin^2\theta}}{n_2 \cos\theta + \sqrt{n_2 - \sin^2\theta}} \cdot \frac{e^{-jk_2 R_2}}{R_2} \\ Q_{asym}^{22} &= \left(\frac{2\cos\theta}{n_2 \cos\theta + \sqrt{n_2 - \sin^2\theta}} - 1\right) \cdot \frac{e^{-jk_2 R_2}}{R_2} \end{aligned} \tag{B9}$$

Note that (B8) is valid when no singularity or branch point is intercepted in the deformation to the steepest descent path [22].